

## Revisiting the Optical Dispersion of Aluminum-Doped Zinc Oxide

### New Perspectives for Plasmonics and Metamaterials

Shabani, Alireza; Khazaei Nezhad, Mehdi; Rahmani, Neda; Mishra, Yogendra Kumar; Sanyal, Biplab; Adam, Jost

*Published in:*  
Advanced Photonics Research

*DOI:*  
10.1002/adpr.202000086

*Publication date:*  
2021

*Document version:*  
Final published version

*Document license:*  
CC BY

*Citation for pulished version (APA):*  
Shabani, A., Khazaei Nezhad, M., Rahmani, N., Mishra, Y. K., Sanyal, B., & Adam, J. (2021). Revisiting the Optical Dispersion of Aluminum-Doped Zinc Oxide: New Perspectives for Plasmonics and Metamaterials. *Advanced Photonics Research*, 2(4), [2000086 ]. <https://doi.org/10.1002/adpr.202000086>

Go to publication entry in University of Southern Denmark's Research Portal

#### Terms of use

This work is brought to you by the University of Southern Denmark.  
Unless otherwise specified it has been shared according to the terms for self-archiving.  
If no other license is stated, these terms apply:

- You may download this work for personal use only.
- You may not further distribute the material or use it for any profit-making activity or commercial gain
- You may freely distribute the URL identifying this open access version

If you believe that this document breaches copyright please contact us providing details and we will investigate your claim.  
Please direct all enquiries to [puresupport@bib.sdu.dk](mailto:puresupport@bib.sdu.dk)

# Revisiting the Optical Dispersion of Aluminum-Doped Zinc Oxide: New Perspectives for Plasmonics and Metamaterials

Alireza Shabani,\* Mehdi Khazaei Nezhad, Neda Rahmani, Yogendra Kumar Mishra, Biplab Sanyal, and Jost Adam\*

Due to the high rate of optical losses and the extensive usage of noble metals, alternative plasmonic materials with maximum tunability and low loss are desired for future plasmonic and metamaterial devices and applications. Herein, the potential of aluminum-doped zinc oxide (AZO), one of the most prominent members of the transparent conducting oxide family, is demonstrated, for its applicability in plasmonic metamaterials. Using first-principles density functional theory, combined with optical calculations, AZO-based, plasmonic split-ring resonators (SRRs) as model examples are showcased. The results match with experimental reports for the optical dielectric functions of pure and 2.08% Al-doped zinc oxide (ZnO), if the Hubbard model to the local density approximation is applied. The broadband optical dispersion data for varying dopant concentrations (0%, 2.08%, and 6.25%) are extracted and provided. The subsequent optical response analyses show the existence of pronounced plasmons and inductor–capacitor modes in Al-doped ZnO SRRs and an enhancement in metallic characteristics and plasmonic performance of AZO upon increasing Al concentration. The findings predict AZO as a low-loss plasmonic material with promising capability for enhancing future optoelectronics applications. The method introduces a new, versatile approach to design future optical materials of arbitrary geometry.

for plasmonics and metamaterial applications and improved optical features compared with noble metals is intensively growing. The role and importance of semiconductors is well known in the optical community for decades. One of the most well-known semiconducting materials, widely used in the creation of various optical instruments, is zinc oxide (ZnO).<sup>[1,2]</sup> Due to its unique features, such as wide direct bandgap at room temperature, large binding energy, high transparency, environment-friendly properties, and, most importantly, low cost and ease of fabrication, it has continuously been a central component of photovoltaic thin films, optoelectronic devices, and even daily applications such as pharmaceuticals and cosmetics.<sup>[3–6]</sup> Hence, an investigation about a direct usage of this compound for plasmonic purposes, via manipulating its material characteristics, provides new horizons for future research and applications.

Metallic behavior occurs when a material's dielectric function real part  $\epsilon_1$  is negative, whereas optical losses occur for a

nonvanishing imaginary part  $\epsilon_2$ . Hence, based on a common plasmonic figure of merit, desirable materials for plasmonic applications comprise a negative real part  $\epsilon_1$ . It has been shown in previous studies that decreasing the damping coefficient and plasmon frequency result in a decrease in  $\epsilon_2$ .<sup>[7–9]</sup> The former directly depends on the degree of structural order such as

## 1. Introduction


In spite of the massive attention plasmonics and metamaterials have gained during the past decades, they are still considered as one of the most interesting branches of physics and optics. Searching for new materials with suitable metallic behavior

Dr. A. Shabani, N. Rahmani, Dr. J. Adam  
Department of Mechanical and Electrical Engineering  
University of Southern Denmark  
Sønderborg DK-6400, Denmark  
E-mail: shabani@sdu.dk; jostadam@sdu.dk

Dr. M. K. Nezhad  
Department of Physics  
Faculty of Science  
Ferdowsi University of Mashhad  
Mashhad 9177948974, Iran

Dr. B. Sanyal  
Department of Physics and Astronomy  
Uppsala University  
Box-516, Uppsala 75120, Sweden

Prof. Y. K. Mishra  
NanoSYD  
Mads Clausen Institute  
University of Southern Denmark  
Sønderborg DK-6400, Denmark

 The ORCID identification number(s) for the author(s) of this article can be found under <https://doi.org/10.1002/adpr.202000086>.

© 2021 The Authors. Advanced Photonics Research published by Wiley-VCH GmbH. This is an open access article under the terms of the Creative Commons Attribution License, which permits use, distribution and reproduction in any medium, provided the original work is properly cited.

DOI: 10.1002/adpr.202000086

crystallinity, existence of dislocations, and impurities, whereas the latter could be achieved by reducing carrier concentration density in metals. One way to access a material with low carrier density (lower than metals), but still having metallic characteristics with small values of  $\epsilon_2$ , is to realize heavily doped semiconductors. In that light, we investigate a member of the transparent conducting oxide (TCO) family, aluminum-doped zinc oxide (AZO), in metamaterial structures. It has been proved that AZO simultaneously shows metallic behavior in  $\epsilon_1$  and low loss or epsilon near zero (ENZ) in  $\epsilon_2$ ,<sup>[10–13]</sup> together with a high potential for optical tunability compared with the conventional metals. Nevertheless, investigations about this compound have been limited to some cases focused on introducing its metallic behavior or using it in the surface plasmon applications (metal–dielectric configurations).<sup>[14–17]</sup> Here, our intention is to show the potential of AZO for the use in future plasmonic devices or metamaterials, by means of combining density function theory (DFT) and the finite-difference time-domain method (FDTD). To this end, we carry out DFT calculations to illustrate the metallic behavior for AZO via electronic density of states (DOS) and optical dielectric functions for the local density approximation (LDA) exchange-correlation functional with and without Hubbard correction (LDA +  $U_d$ ). Using Lorentzian distributions,<sup>[18]</sup> we subsequently extract the optical dispersion parameters (complex dielectric permittivity and refractive index) from our AZO DFT results, together with Drude–Lorentz parameters, highly relevant for any subsequent optical simulation involving these novel materials. As a concrete exemplary demonstration, we finally feed the generated optical dispersion data into an FDTD solver for optical simulations (by the Optiwave package) and simulated the optical response of a square array of u-shaped AZO SRRs. Our results show the presence of electric and magnetic modes in the simulated geometry as a main characteristic feature of SRRs. They further introduce AZO as a material with high potential for plasmonic and metamaterial applications in general, and our procedure proposes a general approach to designing novel, prospective materials specifically tailored for plasmonic applications.

In the following paragraphs, we first present our first-principles approach and DOS analysis of pure and Al-doped ZnO, demonstrating the important influence of Hubbard's correction when modeling members of the TCO family and predicting metallic behavior in (fabricable) compounds with 2.08% and 6.25% doping concentrations. Subsequently, we demonstrate the extraction of dispersive material data from our DFT results, including interpretation, analysis, and verification against experimental data. We provide optical dispersion data and Drude–Lorentz parameters for differently doped (0%, 2.08%, and 6.25%) AZO, to serve in any electromagnetic structure or device simulation. We show, for the first time, the clearly superior optical characteristics in the 6.25% case. Finally, we prove the promising prospect of our generated AZO data for tunable plasmonic metamaterial applications, exemplarily showcasing plasmonic and inductor–capacitor (LC) resonances in SRRs built from differently doped AZO.

## 2. DFT Calculations

### 2.1. Calculation Parameters and Optical Parameter Extraction

We calculate the electronic and optical properties of Al-doped ZnO compounds using first-principles calculations. To this end, we used the SIESTA package<sup>[19]</sup> within LDA, to simulate  $2 \times 2 \times 2$  and  $6 \times 2 \times 2$  supercells of zinc oxide (ZnO), having 16 and 48 zinc (oxygen) atoms (shown in **Figure 1**), respectively. The primitive cell includes a hexagonal wurtzite structure with cell parameters of  $a = b = 3.249$  and  $c = 5.206$  Å, taken from experimental lattice parameters of ZnO.<sup>[20]</sup> To gain an AZO compound with 2.08% and 6.25% of doping, we substituted one Zn atom with Al in the corresponding supercell (**Figure 1**). We further used the Perdew–Zunger (PZ) scheme<sup>[21]</sup> as the exchange-correlation functional, based on the linear combination of atomic orbitals (LCAO) pseudopotential technique. The Monkhorst–Pack scheme,<sup>[22]</sup> over the  $k$ -point grid of  $15 \times 15 \times 10$ , performed the integration in the first Brillouin zone. To optimize the structures, we set the minimum force on every atom and energy

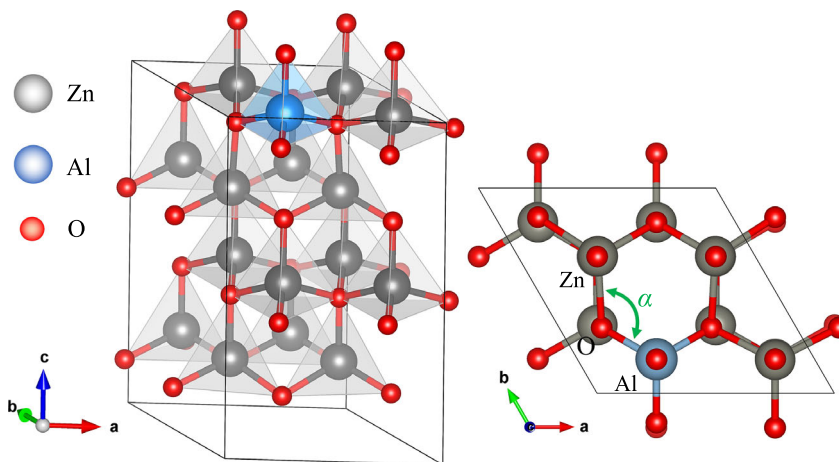


**Figure 1.** a) Wurtzite crystal structure of aluminum-doped zinc oxide (AZO) for  $2 \times 2 \times 2$  supercell (6.25 at% Al doped in ZnO), holding 16 Zn and 16 O atoms in a supercell.

change to  $0.002 \text{ eV}\text{\AA}^{-1}$  and  $10^{-4} \text{ eV}$ , respectively, for a plane wave energy cutoff of 300 Ry. In the field of computational optics, the optical dielectric function and the bandgap are the major quantities to determine the accuracy of calculation, if compared with experimental results. Here, we concentrate on the bandgap as a quantity related to optical material properties. As a result of well-known limitations of standard DFT, using this approach gives rise to an underestimation of the bandgap of many compounds. To describe the exchange and correlation potential more accurately, we therefore adopted the DFT +  $U$  calculation method (Hubbard model). The DFT +  $U$  approach looks to compensate for the relevant shortcoming by adding an orbital-dependent term to the DFT potential. This model is used for highly correlated materials, in which the on-site Coulomb interactions are particularly strong for localized d and f electrons that cause the large Coulomb repulsion between localized electrons not properly treated by a functional such as the LDA or generalized gradient approximation. In earlier studies, it was also shown that applying the correction only to the 3d orbital of Zn leads to the underestimation of the bandgap of ZnO, even for high values of  $U$ . For instance, the bandgap calculated using DFT +  $U_d$  (where  $U_d$  is the correction of the Coulomb repulsion for the d electrons of Zn) was found to be  $\approx 1.5 \text{ eV}$ ,<sup>[23]</sup> which is still far from the value measured in the experimental studies, that is,  $E_{\text{gap\_exp}} = 3.4 \text{ eV}$ .

By investigating the impact of the  $U$  parameter of both p orbital electrons of oxygen ( $U_p$ ) and the d orbital electrons of the transition metal ( $U_d$ ) on optical properties of ZnO, Sheetz et al.<sup>[24]</sup> suggested that the  $U_p$  term should be included in Hubbard model to correct the bandgap. Ma et al. reported that using the value of 10.5 eV for  $U_d$  and 7.0 eV for  $U_p$  in their simulations resulted in an improved bandgap for the studied compounds.<sup>[25]</sup> Calzolari et al. also used the Hubbard model with  $U$  values of 12 and 7 eV for  $U_d$  and  $U_p$ , respectively, yielding results consistent with the experimental results.<sup>[17]</sup> In our calculations, the calculated bandgap of ZnO by the LDA method approximately reads 0.81 eV, which is considerably less than the experimental value of 3.37 eV. To calculate the optical properties of AZO more accurately and better represent the experimental results, we therefore adopted the DFT +  $U_d$  +  $U_p$  method. It turned out that  $U$  values of 14 and 7 eV for  $U_d$  and  $U_p$ , respectively, best agree with the experimental results for the bandgap, DOS, and optical dielectric function.

## 2.2. Results and Discussion

At first, we investigated the structural properties of AZO. Table 1 shows the optimized lattice parameters for the relaxed structure of pure, 2.08, and 6.25 at% Al-doped ZnO, in comparison with previously published results. To avoid complexity, we used a specific abbreviation for different compounds by considering their doping percentage and included the Hubbard model. For instance, AZO0.2 indicates 2.08% Al-doped in ZnO with included Hubbard potential while AZO2 shows the same level of doping but without  $U$  parameter. The same holds for other compounds of the present study. According to our calculations, the lattice parameters of pure ZnO are  $a = 3.215$  and  $c = 5.248$  Å, which are close to the experimental values stated above and in

**Table 1.** The optimized lattice parameters of hexagonal wurtzite crystal structures of ZnO, AZO2, and AZO6 compounds. The Al/Zn–O is the bond length and Zn–O–Zn/Al is the bond angle ( $\alpha$ ) shown in Figure 1b.

	ZnO	AZO2	AZO6
$a$ [Å]	3.215 3.313 <sup>a)</sup> 3.295 <sup>b)</sup> 3.280 <sup>c)</sup>	3.214 3.250 <sup>e)</sup> 3.245 <sup>f)</sup>	3.213 3.312 <sup>a)</sup> 3.271 <sup>c)</sup> 3.270 <sup>d)</sup>
$c$ [Å]	5.248 5.329 <sup>a)</sup> 5.330 <sup>c)</sup>	5.247 5.240 <sup>e)</sup> 5.178 <sup>f)</sup>	5.245 5.315 <sup>a)</sup> 5.334 <sup>c)</sup> 5.290 <sup>d)</sup>
$c/a$	1.632	1.632	1.632
Zn–O [Å]	1.968	–	–
Al–O [Å]	–	1.802	1.810
Zn–O–Zn ( $\alpha$ ) [deg.]	109.491	–	–
Zn–O–Al ( $\alpha$ ) [deg.]	–	114.054	113.560

<sup>a)</sup>Ref. [26]; <sup>b)</sup>Ref. [27]; <sup>c)</sup>Ref. [28]; <sup>d)</sup>Ref. [29]; <sup>e)</sup>Ref. [30]; <sup>f)</sup>Ref. [31].

agreement with other theoretical calculations.<sup>[26–31]</sup> In case of doped ZnO, the relaxed parameters are  $a = 3.214$  Å and  $c = 5.247$  Å for AZO2 and  $a = 3.213$  Å and  $c = 5.245$  Å for AZO6, which show a decrease of the lattice parameters and cell volume of AZO compounds compared with pure ZnO upon increasing doping level. In pure ZnO, each Zn atom is surrounded by three oxygen neighbors in the a–b plane and one in the c-direction. By doping with the Al atom, a reduction in the bond length of Al–O is seen, in comparison with the Zn–O bond in pure ZnO. Moreover, the bond angle between Zn–O–Al (shown by  $\alpha$ ) increases in the case of AZO2 and AZO6. These show that oxygen atoms situated in the neighborhood of Al suffer from displacement and deflection as they get closer to the Al atom, which is shown in Figure 1b.<sup>[32]</sup> In fact, Al doping results in a mismatch in the crystal structure of ZnO, mainly due to the significant difference between the ionic radii (0.53 and 0.75 Å for  $\text{Al}^{3+}$  and  $\text{Zn}^{2+}$ , respectively) and the electronegativity of Al and Zn atoms. The mentioned results imply that  $\text{Zn}^{2+}$  ions are replaced by  $\text{Al}^{3+}$  ions in the ZnO lattice.

Figure 2 shows total and partial DOS for pure and Al-doped ZnO. To avoid the complexity, we have only depicted the partial density of states (PDOS) for the compounds with included  $U$  parameter. It becomes clear that ZnO is a semiconductor with a bandgap of 0.9 eV; however, the LDA calculations always underestimate the bandgap compared with experimental values. By doping Al into ZnO, the Fermi level shifts upward into the conduction band in the case of AZO2, indicating typical n-type doping in AZO2 and revealing the role of Al as a donor in this compound. This is because of one more valence state of group III elements such as  $\text{Al}^{3+}$  and  $\text{Ga}^{3+}$ , in comparison with  $\text{Zn}^{2+}$ , which injects one excessive electron to the conduction band, increases the conductance of ZnO, and provides the metallic characteristics. The enhanced conductance seen in ZnO upon doping with Al gives the motivation for evaluating the potential application of this compound in plasmonics and metamaterials. In the AZO6 DOS, we see a further shift, indicating that more electrons accumulated in the Fermi level, therefore, an enhanced

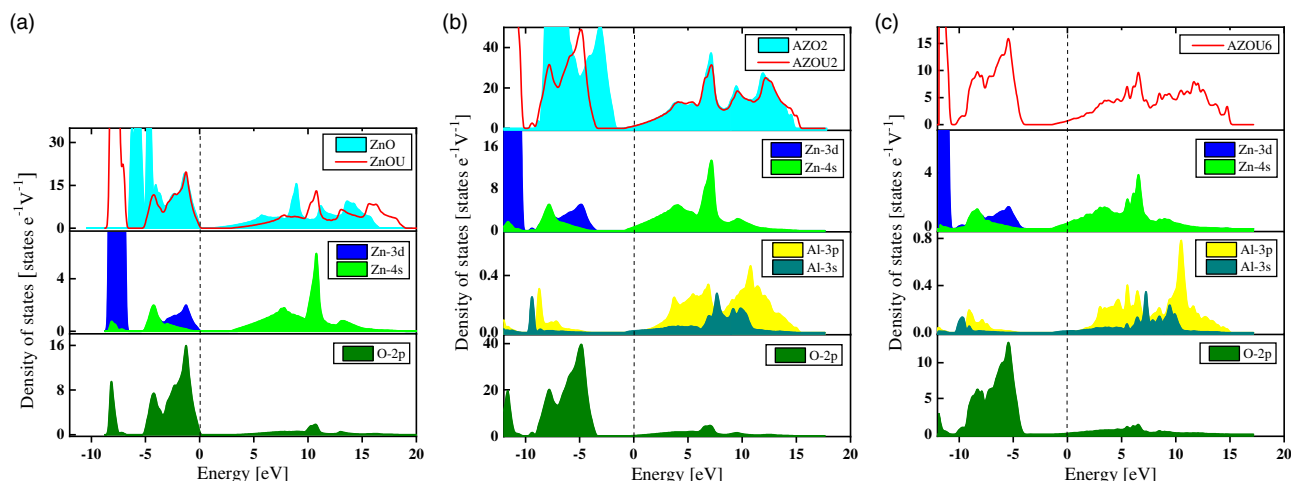


**Figure 2.** The calculated DOS and PDOS of a) ZnO, b) AZO2, and c) AZO6 with and without the Hubbard model ( $U$ ). The PDOS curves are only depicted for the compounds with Hubbard correction included. The Fermi level was set at zero energy.

metallic behavior. In addition, we observe a blue shift in the optical bandgap of ZnO with higher Al content. We attribute this to the excessive electrons provided by Al, occupying the states from the bottom of the conduction band to the Fermi level, creating an  $\epsilon_2$  plateau with an edge at 2 eV. By a further increase in energy,  $\epsilon_2$  grows gradually and reaches a maximum at 7 eV. This maximum is attributed to the second biggest peaks in the DOS, starting at  $-7$  eV.

A further look at the DOS of ZnO also reveals that the upper valence band mainly comprises the mixture of Zn-3d and O-2p states, whereas the bottom of the conduction band is due to the Zn-4s state. Note that in low doping concentration, the crystalline order of ZnO is only slightly perturbed. This causes Al not to produce the defect states in the ZnO bandgap. In fact, the key role of Al is to shift the Fermi energy and provide conductive carriers in the conduction band.

By applying the  $U$  parameter, the bottom of the conduction band of ZnO shifts to higher energies and an increase in the bandgap occurs due to the impact of the Zn-3d and O-2p orbitals (on-site repulsion). For ZnOU, the upper-valence-band orbitals are mainly Zn-3d and O-2p, whereas the conduction band is predominately occupied by the Zn-4s state, mixed with a few O-2p states. The distribution of states is broader in the range from 0 to  $-5.5$  eV and localized around  $-7.5$  eV. The  $U$  parameter does not affect the states around the Fermi energy, as shown by the upper valence band still remaining unchanged. Upon Al doping, the Fermi level shifts upward, into the conduction band, and crosses the DOS of AZO2 and AZO6, because of an excessive valence state of Al compared with Zn, which induces n-type conductive characteristics for AZO. Similar to ZnOU, we notice a larger energy difference between the valence and conduction bands, as compared with compounds without Hubbard potential, which technically gives rise to the results closer to the literature.

Upon doping Al into ZnO, the DOS crosses the Fermi energy level in the case of AZO2, indicating metallic behavior. It causes an infinite response to appear in the near-zero energy region, called intraband transition and formulized by the Drude model. The intraband spans to 1 eV, exactly where the DOS decreases, and reaches a minimum value around  $-1$  eV. The reason for seeing such a reducing trend till 1 eV in  $\epsilon_2$  of AZO2 is that by getting away from the Fermi level, the DOS decreases till  $-1$  eV

(Figure 2), resulting in a reduction in electron transition rate from occupied to empty states. At the energy range between  $-3$  and  $-1.5$  eV, the DOS starts increasing abruptly, creating an  $\epsilon_2$  plateau with an edge at 2 eV. By a further increase in energy,  $\epsilon_2$  grows gradually and reaches a maximum at 7 eV. This maximum is attributed to the second biggest peaks in the DOS, starting at  $-7$  eV.

### 3. Extracting Optical Quantities from DFT Calculations

To extract optical dispersion data from the compounds found in the previous section, we used an optical mesh of  $50 \times 50 \times 50$  mesh cells to calculate the optical dielectric function for an incident unpolarized electromagnetic wave from the integral of momentum matrix elements between the occupied and empty states around the Fermi level, given by Liu et al.<sup>[33]</sup>

$$\epsilon_2(\omega) = \frac{Ve^2}{2\pi\hbar m^2 \omega^2} \int d^3k \sum_{ij} |\langle \mathbf{K}_i | P | \mathbf{K}_j \rangle|^2 f(K_i)(1 - f(K_j)) \times \delta(E_{K_i} - E_{K_j} - \hbar\omega) \quad (1)$$

where  $P$  is the electron momentum operator,  $\hbar\omega$  is the energy of the incident photon,  $f(K_i)$  is the Fermi function,  $e$  is the electric charge,  $m$  is the electron mass,  $V$  is the volume of the first Brillouin zone, and  $|\mathbf{K}_i\rangle$  and  $|\mathbf{K}_j\rangle$  denote filled initial and empty final states, respectively. Furthermore,  $\delta$  indicates Dirac's delta distribution,  $\omega$  is the irradiation frequency, and  $E_{K_i}$  and  $E_{K_j}$  stand for the energy of initial and final states. Formula (1) connects the optical and the electronic properties of a material. We subsequently evaluated the dielectric function real part  $\epsilon_1(\omega)$  from the imaginary part  $\epsilon_2(\omega)$  by Kramers-Kronig<sup>[34,35]</sup> transformation.

To validate our calculations, we compared the DFT-extracted real and imaginary parts of the dielectric function to literature-based experimental reports (Figure 3). Apparently, the absorption edge in "regularly calculated" ZnO starts at around



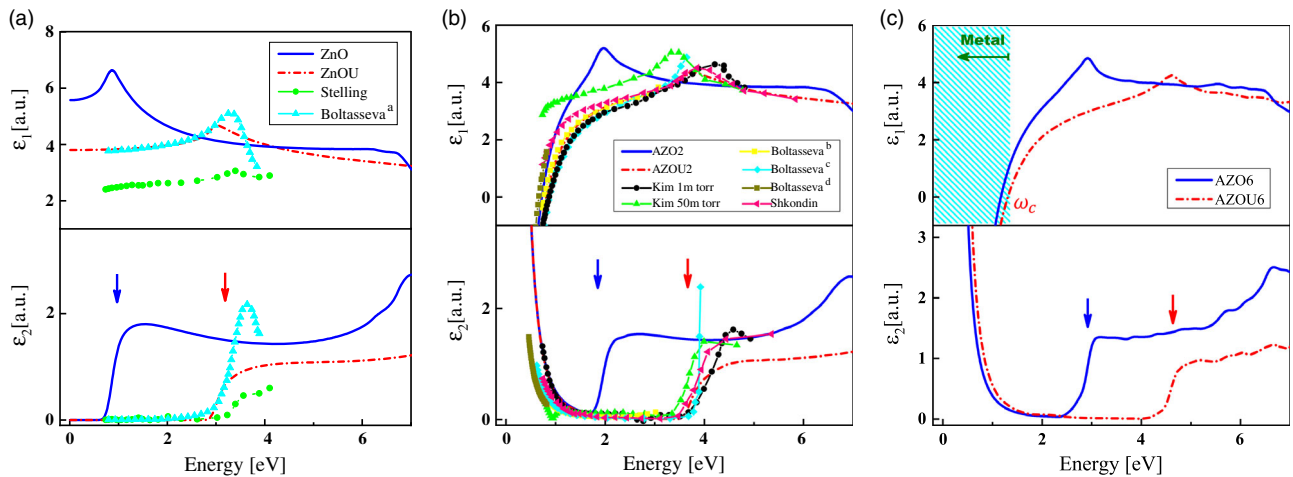


**Figure 3.** Real and imaginary parts of dielectric functions for a) pure and b) Al-doped ZnO. Experimental data were taken from literature (Boltasseva<sup>a</sup>,<sup>[47]</sup> b<sup>[48]</sup> c [7] d [10] Kim,<sup>[49]</sup> Shkondin,<sup>[31]</sup> Stelling<sup>[50]</sup>). The arrows show the interband transition edges. The hatched area in c) AZO6 indicates the region with metallic behavior.

0.9 eV, which is completely inconsistent with the experimental reports. Applying the  $U$  parameter introduced in the previous section causes the edge to blue shift in the ZnOU case, consequently creating results much closer to the experimental reports, with an optical bandgap of 3.1 eV. It is worth mentioning that only the interband transitions contribute in the dielectric functions, as a result of the semiconducting behavior of ZnO.

The  $U$  parameter further shifts the dielectric function of AZO2, pushing the AZO2 absorption edge to around 4 eV, perfectly matching the majority of experimental reports. We address this shift of the upper valence bands of AZO2 to lower energies to the fact that the incident light beam requires more energy to excite electrons for interband transitions. AZO2 exhibits the lowest optical loss at the energy range from 1.5 to 3.5 eV, due to the ENZ characteristics, rendering it a transparent material in the vis–NIR, with potential application in negative-refractive-index metamaterials, operating in the NIR. This confirms the fact about the TCO family that in the NIR region, where they exhibit metallic behavior, the imaginary part of the dielectric function is several times smaller than that for Ag, which has the smallest material loss among metals.<sup>[9]</sup> Comparing the DOS and  $\epsilon_2$  diagrams of pure and Al-doped ZnO (Figure 2 and 3), we conclude that, as there is approximately the same shape for the DOS of two compounds, the  $\epsilon_2$  plots are relatively identical, except an additional part in AZO due to metallic characteristics. Upon increasing the doping level, the absorption edge of the dielectric function further blue shifts, as a result of pushing the valence bands away from the Fermi energy in DOS of 6.25% Al doping (Figure 3c). We also see an opened gap by applying the Hubbard correction, rendering AZO6 a better material for ENZ characteristics, with a more extended domain.

Consequently, having metallic behavior with a smaller plasmon frequency compared with the noble metal due to low carrier concentrations, as well as a low rate of Drude damping, makes AZO interesting for use in plasmonics (metamaterials). To support this claim, in the following paragraphs, we will investigate the plasmonic potential of the two proposed AZO compounds,

with included Hubbard correction in an SRR cell, and study whether or not increasing the doping level is able to enhance the optical performance in such systems. Furthermore, this also embodies a proper example showing how our suggested method works and will provide a better insight into how DFT, combined with optical simulations like FDTD, can be used to fully predict the optical features of materials in a specific geometry. To this end, we extract and supply analytic fitting parameters for use in optical simulations (where a direct approximation of dielectric functions is impossible). We applied the Drude–Lorentz model (Equation (2)<sup>[36]</sup>) to the dielectric function calculated by DFT, to extract the optical quantities required for the FDTD simulations. The model includes intraband transitions of free electrons as well as interband transitions as a quantum mechanical effect

$$\epsilon(\omega) = \epsilon_{\infty}(\omega) + \sum_j \frac{f_j \omega_p^2}{(\omega_j^2 - \omega^2) - i\omega\gamma_j} \quad (2)$$

Here,  $\omega_j$ ,  $\gamma_j$ , and  $f_j$  are resonance frequency, damping coefficient, and resonance strength, respectively. The background permittivity is denoted by  $\epsilon_{\infty}$  and  $\omega_p$  is the plasma frequency. Upon fitting the imaginary part of dielectric function by Lorentzian distributions (Figure 4) we obtained the Drude–Lorentz model parameters for AZO2 and AZO6 cases. We used ten and nine Lorentzian distributions to obtain fitted curves with proper orders of accuracy. The corresponding results are also shown in Table 2. The DFT calculations directly reveal plasmon frequencies of 1.515 and 2.193 eV for AZO2 and AZO6, respectively. Note that the first resonance in both cases corresponds to the Drude model, with the damping coefficient taken from a study by Naik et al.<sup>[11]</sup> as an empirical quantity. This coefficient is inversely proportional to the average time between subsequent collisions of free electrons (relaxation time) and it describes the loss mechanism in the conduction electrons of metals via scattering, by defects, surface states, and lattice vibrations. Moreover, we display the real and imaginary parts of the thereby calculated refractive index (Insets of Figure 4), which can be used

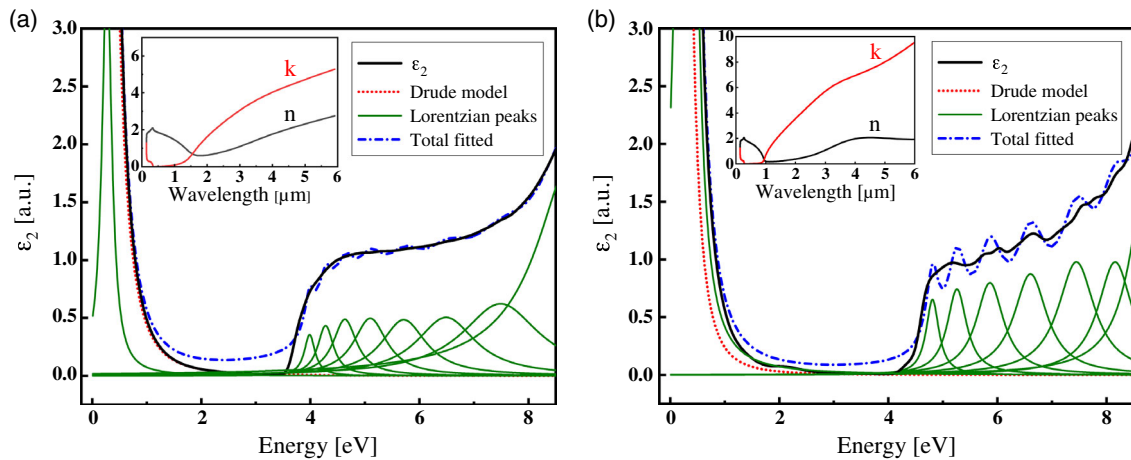


**Figure 4.** Drude–Lorentz model fitted to the a) AZOU2 and b) AZOU6 imaginary part of dielectric functions, to extract optical parameters for FDTD simulations. The corresponding refractive index and absorption coefficient are shown in the insets.

**Table 2.** Optical parameters of Drude–Lorentz model for AZOU2 and AZOU6 with  $U_d$  and  $U_p$  values of 14 and 7 eV, respectively.

Resonance	AZOU2			AZOU6		
	$\omega_j$ [eV]	$\gamma_j$ [eV]	$f_j$	$\omega_j$ [eV]	$\gamma_j$ [eV]	$f_j$
1	0	0.2	1	0	0.05	1
2	0.269	0.216	0.088	0.294	0.213	0.243
3	3.986	0.240	0.148	4.810	0.286	0.186
4	4.280	0.352	0.284	5.258	0.433	0.351
5	4.634	0.527	0.519	5.863	0.613	0.597
6	5.098	0.742	0.819	6.607	0.741	0.890
7	5.712	0.998	1.204	7.449	0.816	1.237
8	6.489	1.317	1.882	8.159	0.772	1.281
9	7.495	1.724	3.508	8.790	0.791	2.728
10	8.879	1.697	12.810	–	–	–

in any kind of optical simulation that admits for a direct import of the (complex) refractive index.

## 4. Exemplary FDTD Simulations for SRRs

### 4.1. Simulation Parameters

We used the Optiwave FDTD package to simulate a periodic cell containing four u-shaped SRRs of AZO in a square array (shown in **Figure 5**). We calculated the optical transmission spectrum for resonators of size  $S$  and periodic lattice constant  $a$  (in all simulations  $a = 1.75 S$ ). The thickness of AZO SRRs was 10 nm.

We irradiated the system by a Gaussian-modulated continuous electromagnetic wave, with time offset of  $4e-15$  s and half width  $0.8e-15$  s, polarized in  $x$ - and  $y$ -directions [transverse magnetic (TM) and transverse electric (TE) incident waves] and propagated along the  $z$ -direction. We applied periodic boundary conditions in  $x$ - and  $y$ -directions, to account for the lattice arrangement, and absorbing boundary conditions, i.e., perfectly

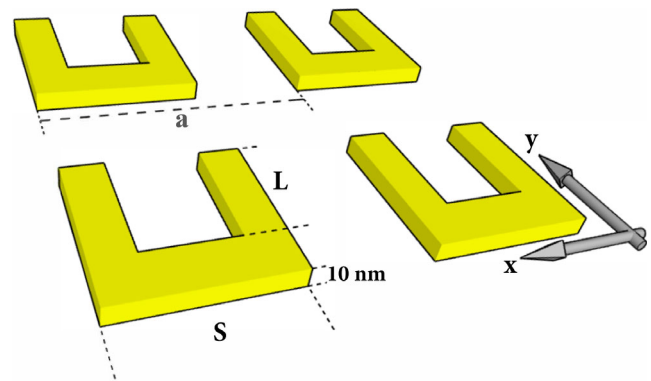


**Figure 5.** A schematic of a cell containing a square array of four u-shaped AZO SRRs. The periodic lattice constant and size of resonators are shown by  $a$  and  $S$ , respectively.

matched layers (PMLs), in  $z$ -direction. Convergence and stability of calculations revealed a mesh size of 4 nm along the  $x$ -,  $y$ -, and  $z$ -axes.

### 4.2. AZO SRRs: The Impact of AZO Doping Concentration

**Figure 6** shows the optical transmission spectrum of a periodic cell including 85 nm-sized u-shaped SRRs, for AZOU2 and AZOU6 (including the Hubbard correction) as the constituent materials. When exposed to a horizontally polarized incident beam (TM), two main dips appear in the transmission spectrum, corresponding to the lowest orders of magnetic modes excited in the system, which are more visible in AZOU6.<sup>[37–39]</sup> The first resonance, excited at wavelengths at around  $4 \mu\text{m}$  for AZOU6 and above  $6 \mu\text{m}$  for AZOU2, is known as the fundamental magnetic SRR mode, because it requires the lowest energy to be excited. Based on this reason, another magnetic mode, appearing at higher energies,  $2 < \lambda < 3 \mu\text{m}$  for AZOU6 and  $3 < \lambda < 4 \mu\text{m}$  for AZOU2, is considered as the first excited magnetic mode.

In the fundamental magnetic resonance, an electric dipole moment appears across the tips of vertical arms, which stems from coupling between the oscillating electric field and the

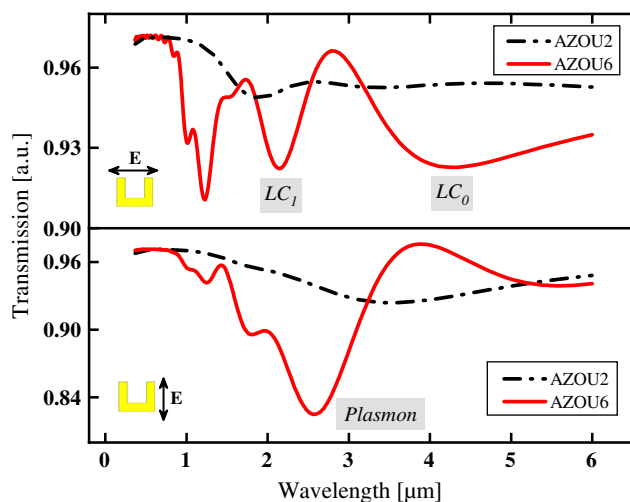


**Figure 6.** The calculated optical transmission spectra of 85 nm-sized u-shaped SRRs for the proposed AZOU2 and AZOU6 compounds as the constituting material. Plasmon and LC modes are clearly excited in the system.

vertical resonator arms. The opposite charges produced by the electric dipole moment induce a circulating current within the resonator, which results in a magnetic dipole moment normal to the SRR plane. Hence, these modes are usually known as the magnetic mode of system. In fact, the negative permeability ( $\mu < 0$ ), which is seen in metamaterial structures, originates from these magnetic characteristics of SRRs. In addition, the optical resonance behavior could be modeled by an equivalent LC resonance circuit, in which the capacitance behavior occurs in the gap region between two parallel arms, whereas the three edges of the u-shaped SRRs play the role of inductance. Therefore, the fundamental and first excited magnetic modes are known as the zeroth and first-order LC resonances,  $LC_0$  and  $LC_1$ , respectively. We labeled these two modes in the top panel of Figure 6. In addition to the main resonances, a few weak dips appeared within the region of study for AZOU6 stemming from the interaction between adjacent SRRs, which is probably not seen for a single SRR with the given amount of the lattice periodic constant, where the SRR cannot feel the impacts of neighbors.

We attribute the resonance shown in the bottom panel of Figure 6, ranging between  $\lambda = 2$  and  $3 \mu\text{m}$  for AZOU6 and the weaker and broader one at higher wavelengths for AZOU2, to the fundamental electric mode of system.<sup>[40,41]</sup> In this resonance, two aligned electric dipole moments are excited around the vertical arms. This mode is associated with the surface plasmon phenomenon occurring at the AZO–dielectric interface, in which coupling between conducting electrons and oscillating electromagnetic waves results in an electric field confinement and enhancement. This phenomenon is also called the plasmonic mode. The plasmonic mode wavelength is always shorter than the one of the  $LC_0$  mode and longer than the one corresponding to the  $LC_1$  mode. The excitation of electric and magnetic modes, with different input waves (TM and TE), shows the polarization-dependent nature of SRRs.

We clearly see that the plasmon and LC modes are stronger in AZOU6 than the ones in AZOU2. In fact, the transmission plot of AZOU2 is rather similar to ZnO, expect for a few weak dips, implying the metallic nature due to Al doping. Figure 6 also shows that, by increasing the doping level to 6.25%, the metallic characteristic grows, as higher plasmonic performance is achieved. This is also confirmed in other dips (not LC and plasmon dips), where the interaction between modes leads to the excitation of other minor resonances in the case of AZOU6.

From the viewpoint of material characteristics, the optical loss fully appears in the imaginary part of the dielectric function and is directly associated with the contributions from the Drude damping coefficient, the plasmon frequency, and interband transitions. Figure 3b,c shows that the interband contributions in both AZOU2 and AZOU6 are similar and, therefore, the contribution is minor. On the other hand, based on the experimental reports in the study by Naik et al.,<sup>[11]</sup> by increasing doping concentration, the Drude damping coefficient decreases from 0.2 to 0.05 for AZOU2 and AZOU6, respectively, giving rise to a reduction in the optical loss. Although the increased plasmon frequency from 1.515 eV for AZOU2 to 2.193 eV for AZOU6 increases the amount of  $\epsilon_2$ , due to more injected electrons, it is found from a simple calculation that the overall optical loss decreases in case of AZOU6 because the damping coefficient contribution predominates the impact of plasmon frequency. Therefore, we conclude that the plasmonic figure of merit in an AZO compound increases upon doping with Al atoms; however, it is not a general rule because more injected free electrons into the system may reversely cause the optical loss to increase due to the direct dependency of  $\epsilon_2$  to the value of plasmon frequency in a metal. Moreover, we see that the resonance modes in AZOU6 blue shift as compared with the ones in AZOU2, indicating a higher amount of plasmon frequency due to more free electrons, as a result of the metallic dopant, showing the tuning capability of AZO in optical response.

### 4.3. AZO SRRs: The Impact of Geometry

In the following paragraphs, we intend to figure out the impact of SRR geometrical parameters on the overall optical response. Due to the remarkable results in the previous section and the consequence that the excited resonances are more pronounced, we focus this analysis on SRRs made of AZOU6.

Figure 7 shows the optical transmission spectra of AZOU6 SRRs with respect to varied sizes of u-shaped SRRs ( $x$ -direction extent  $S$ ). It is visible that, by increasing size of SRRs from 70 to 100 nm, the LC modes red shift to higher wavelengths. By growing the arm length, a larger resonator area lies in the magnetic field, giving rise to the enhancement in magnetic flux and subsequently in self-inductance of the circuit ( $L$ ). In contrast, the system capacitance is not influenced by the alteration of resonator's dimension. The distance and area of two parallel plates (vertical arms) simultaneously change. Hence, according to the capacitance of a plane capacitor, these two effects cancel each other. This implies that the SRR dimension impact could be ignored on the capacitor behavior. Consequently, according to the equation for resonance wavelength of an LC circuit,  $\lambda_{\text{res}} = 2\pi c\sqrt{LC}$ ,



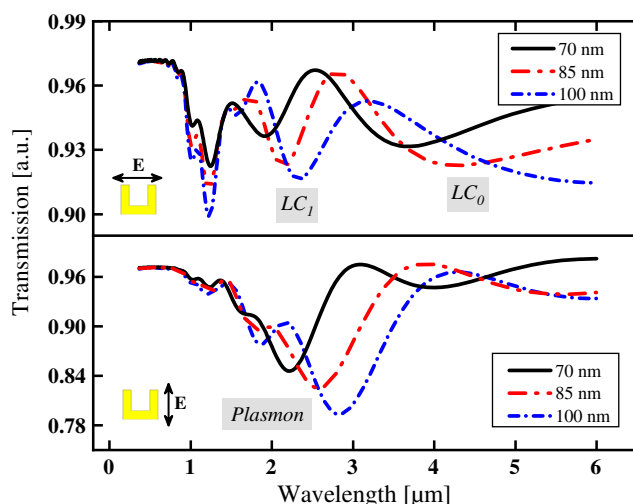


**Figure 7.** Optical transmission spectra calculated for the proposed AZOU6 SRRs with respect to differently sized resonators.

enlarging the resonator size and causing the LC peak to shift to higher wavelengths.

Upon increasing the size of SRRs, the plasmonic mode undergoes a red shift. It is well known that the plasmonic resonance wavelength in such structures is proportional to the length of the resonator, parallel to the incident beam polarization.<sup>[42,43]</sup> In the case of an incident beam with TE polarization, as the light is linearly polarized along the  $y$ -axis (bottom panel of Figure 7), increasing the vertical arm length directly increases the efficient oscillation length of electrons confined to the vertical arms. In other words, increasing the vertical arms of SRRs causes the electric dipole moments to excite at lower energies, corresponding to longer plasmonic mode wavelengths. It is worth mentioning that in a metamaterial system, comprising periodic arrays of metal wires and SRRs, each one of the wires and SRRs possesses a unique plasmon mode, because of their metallic characteristics, whereas the final amount of the plasmon mode for the metamaterial system is obtained by considering a coupling taking place between these two modes.<sup>[44]</sup> Moreover, Figure 7 shows that for both TE and TM polarizations, as the size of SRRs decreases further, the kinetic inductance starts to set in and the optical loss increases, which gradually diminishes the resonance contrast.

We also observe that the metallic characteristics of AZOU6 (lossy nature), arising in the form of a reduction for the intensity of the transmitted beam, starts at  $\lambda = 950$  nm, as expected from the AZOU6  $\epsilon_1$  diagram (Figure 3c, hatched area), where the crossover frequency, at which the real part of the dielectric function becomes zero, is  $\omega_c = 1.3$  eV.

To further investigate the impact of geometrical parameters on the optical behavior of AZO SRRs, we designed another optical simulation, in which the optical transmission spectrum of an array of SPRs was calculated with respect to different lengths of vertical arms ( $L$ ), ranging from zero (a simple rod) to 60 nm (a complete resonator). The simulations comprised 85 nm-sized resonators as all geometrical parameters were fixed, except for the vertical arms (geometry sketch on top of Figure 8). We

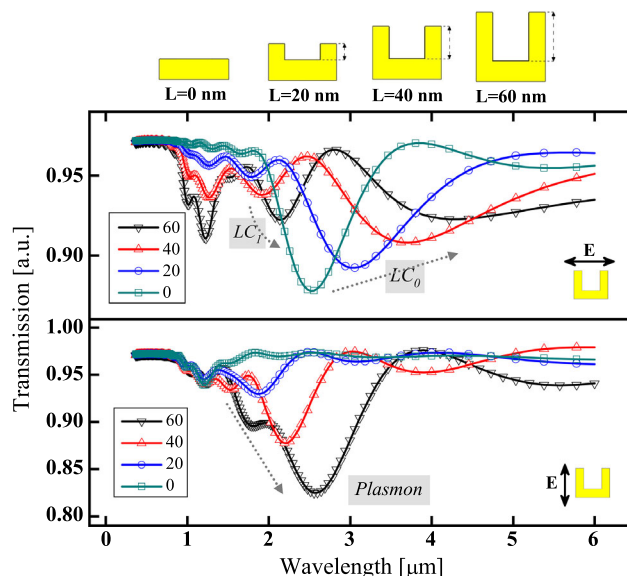


**Figure 8.** The calculated optical transmission spectra of AZOU6 SRRs with respect to different lengths of the vertical arm (top panel) for 85 nm-sized resonators.

irradiated the SRRs under TM- and TE-polarized incident beams. We see that both  $LC_0$  and  $LC_1$  modes were excited in TM polarization even for a simple rod (Figure 8). It is due to this fact that a simple rod could show capacitor behavior, stemming from the accumulation of opposite charge particles at the end of each side. Moreover, upon growing vertical arms from the simple rod to 60 nm, the resonance wavelength of both  $LC_0$  and  $LC_1$  increases. This behavior is consistent with the aforementioned equation for the wavelength of LC resonance in a circuit that growing the vertical arms of SRRs increases the area of two parallel plates, resulting in an increase in the capacitance of SRRs, which subsequently leads to the red shift for the LC modes. We observe the same behavior for TE polarization upon increasing the vertical arm length: the longer the vertical arms, the larger the effective length for electrons, leading to longer plasmonic wavelengths. Even an excited plasmon mode (weak) is visible for the simple rod because of transverse mode coupling in this case, in which the rod thickness provides an effective length, however short, for oscillating electrons.

To confirm the obtained results and show that the observed transmission dips arise from the excitation of the zeroth and first order of LC modes in the TM wave as well as the plasmon mode in TE, we plotted the electromagnetic field profiles on the surface of u-shaped SRRs. Figure 9 shows the magnitudes of  $E_x$ ,  $E_y$ , and  $H_z$  for the 85 nm-sized SRRs, in Figure 6, at the wavelengths of  $\lambda = 2.14$  and  $4.28$   $\mu\text{m}$ , corresponding to the  $LC_1$  and  $LC_0$  resonances, and  $\lambda = 2.58$   $\mu\text{m}$  for the plasmon resonance. It is clear that the accumulated charges on the tips of vertical arms in the  $LC_0$  (the points where  $E_x$  and  $E_y$  were concentrated) formed an electric dipole moment and subsequently a loop current in SRR, which induced a magnetic moment normal to the SRR plane, as shown in  $H_z$  field distribution.<sup>[45,46]</sup> In the  $LC_1$  mode,  $E_x$  and  $E_y$  concentrated on both vertical and horizontal arms, showing that the symmetry was broken in this case and two

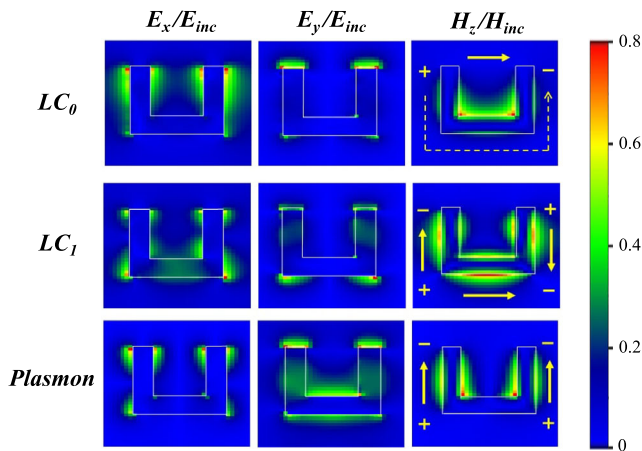


**Figure 9.** Calculated relative electric and magnetic field amplitudes, for 85 nm-size AZOU6 SRRs, where  $E_{inc}$  and  $H_{inc}$  denote the incident electric and magnetic field amplitudes, respectively. The yellow arrows indicate electric dipole moments. The LC modes are associated with polarization along the horizontal arm whereas the plasmon mode was excited in the polarization parallel to the side arms.

anti-parallel electric dipole moments were induced in the vertical arms. This formed a delocalized  $H_z$  which is out of SRR compared with the  $LC_0$  mode. In the case of the plasmon mode, two parallel electric dipole moments are seen around vertical arms in the  $H_z$  profile, resulting in a symmetric mutual coupling between these two dipoles. It indicates that TM polarization could not provide a plasmon mode excitation due to symmetry considerations. It should be also noted that due to the SRRs configuration of present study, not all SRRs contribute in the LC or plasmon mode excitation as some of them remain inactive in the unit cell. This shortcoming can be improved using higher order-symmetric geometries.

## 5. Conclusion

In the present work, we presented a new method, using a combination of DFT and optical calculations, to investigate the potential of AZO for being used in optical metamaterial and plasmonic applications (exemplified via FDTD calculations for optical lattices of SRRs). Our DFT calculations with the LDA +  $U$  exchange-correlation functional revealed a corrected bandgap value of 3.3 eV for pure ZnO as well as metallic characteristics for AZO, which match recent experimental reports. We fitted the calculated imaginary part of the dielectric function of AZO with 2.08% and 6.25% of Al impurities by Lorentzian distributions, and our calculations provide dielectric dispersion curves (complex refractive index and permittivity), to be used in any subsequent optical calculation. Our exemplary FDTD-calculated optical transmission spectrum results in a square array of u-shaped SRRs, made of the proposed AZO compounds, and predicts the presence of excited electric and magnetic modes for both Al doping concentrations, as the main characteristic feature of SRRs. Our findings show pronounced excited modes for the 6.25% AZO case, indicating an improved metallic characteristic upon increasing the doping level. Our numerical results suggest

AZO as a compound with potential tunability upon alteration of geometrical parameters and material engineering for future plasmonic applications.

## Acknowledgements

This work was partly funded by Interreg Deutschland–Danmark with money from the European Regional Development Fund, project numbers 086-1.1-17 (CheckNano) and 096-1.1-18 (Access and Acceleration).

## Conflict of Interest

The authors declare no conflict of interest.

## Keywords

Al-doped ZnO, density function theory, finite-difference time domains, Hubbard correction, plasmonics, split-ring resonators, transparent conducting oxides

Received: October 5, 2020

Revised: December 4, 2020

Published online: February 9, 2021

- [1] Y. K. Mishra, R. Adelung, *Mater. Today* **2018**, 21, 631.
- [2] D. P. Norton, Y. W. Heo, M. P. Ivill, K. Ip, S. J. Pearton, M. F. Chisholm, T. Steiner, *Mater. Today* **2004**, 7, 34.
- [3] P. Steiger, J. Zhang, K. Harrabi, I. A. Hussein, J. M. Downing, M. A. McLachlan, *Thin Solid Films* **2018**, 645, 417.
- [4] K. P. Ong, D. J. Singh, P. Wu, *Phys. Rev. B* **2011**, 83, 115110.
- [5] F. M. Chang, S. Brahma, J. H. Huang, Z. Z. Wu, K. Y. Lo, *Sci. Rep.* **2019**, 9, 1.
- [6] J. Zhou, N. S. Xu, Z. L. Wang, *Adv. Mater.* **2006**, 18, 2432.
- [7] G. V. Naik, V. M. Shalae, A. Boltasseva, *Adv. Mater.* **2013**, 25, 3264.
- [8] P. R. West, S. Ishii, G. V. Naik, N. K. Emani, V. M. Shalae, A. Boltasseva, *Laser Photonics Rev.* **2010**, 4, 795.
- [9] A. Boltasseva, *MRS Bull.* **2014**, 39, 461.
- [10] G. V. Naik, J. Liu, A. V. Kildishev, V. M. Shalae, A. Boltasseva, *Proc. Natl. Acad. Sci.* **2012**, 109, 8834.
- [11] G. V. Naik, J. Kim, A. Boltasseva, *Opt. Mater. Express* **2011**, 1, 1090.
- [12] Y. Wang, A. Capretti, L. D. Negro, *Opt. Mater. Express* **2015**, 5, 2415.
- [13] M. A. Noginov, L. Gu, J. Livenere, G. Zhu, A. K. Pradhan, R. Mundle, M. Bahoura, Y. A. Barnakov, V. A. Podolskiy, *Appl. Phys. Lett.* **2011**, 99, 021101.
- [14] T. Gric, A. Gorodetsky, A. Trofimov, E. Rafailov, *J. Infrared Millimeter Terahertz Waves* **2018**, 39, 1028.
- [15] J. Y. Lin, K. D. Zhong, P. T. Lee, *Opt. Express* **2016**, 24, 5125.
- [16] A. K. Pradhan, R. M. Mundle, K. Santiago, J. R. Skuza, B. Xiao, K. D. Song, M. Bahoura, R. Cheaito, P. E. Hopkins, *Sci. Rep.* **2014**, 4, 6415.
- [17] A. Calzolari, A. Ruini, A. Catellani, *ACS Photonics* **2014**, 1, 703.
- [18] A. Shabani, M. K. Nezhad, N. Rahmani, M. R. Roknabadi, M. Behdani, B. Sanyal, *Plasmonics* **2019**, 14, 1871.
- [19] J. M. Soler, E. Artacho, J. D. Gale, A. García, J. Junquera, P. Ordejón, D. S. Portal, *J. Phys.: Condens. Matter* **2002**, 14, 2745.
- [20] R. D. Vispute, V. Talyansky, S. Choopun, R. P. Sharma, T. Venkatesan, M. He, X. Tang, J. B. Halpern, M. G. Spencer, Y. X. Li, L. G. Salamanca-Riba, *Appl. Phys. Lett.* **1998**, 73, 348.
- [21] J. P. Perdew, A. Zunger, *Phys. Rev. B* **1981**, 23, 5048.

- [22] H. J. Monkhorst, J. D. Pack, *Phys. Rev. B* **1976**, 13, 5188.
- [23] A. Stashans, K. Olivos, R. Rivera, *Phys. Scr.* **2011**, 83, 065604.
- [24] R. M. Sheetz, I. Ponomareva, E. Richter, A. N. Andriotis, M. Menon, *Phys. Rev. B* **2009**, 80, 195314.
- [25] X. Ma, B. Lu, D. Li, R. Shi, C. Pan, Y. Zhu, *J. Phys. Chem. C* **2011**, 115, 4680.
- [26] M. Wu, D. Sun, C. Tan, X. Tian, Y. Huang, *Materials* **2017**, 10, 359.
- [27] X. M. Duan, C. Stampfl, M. M. M. Bilek, D. R. McKenzie, *Phys. Rev. B* **2009**, 79, 235208.
- [28] A. Slassi, S. Naji, A. Benyoussef, M. Hamedoun, A. E. Kenz, *J. Alloys Compd.* **2014**, 605, 118.
- [29] Y. Zhao, H. Yang, B. Yang, Z. Liu, P. Yang, *Sol. Energy* **2016**, 140, 21.
- [30] A. A. Al-Ghamdi, O. A. Al-Hartomy, M. E. Okr, A. M. Nawar, S. El-Gazzar, F. El-Tantawy, F. Yakuphanoglu, *Spectrochim. Acta Part A Mol. Biomol. Spectrosc.* **2014**, 131, 512.
- [31] E. Shkondin, O. Takayama, M. A. Panah, P. Liu, P. V. Larsen, M. D. Mar, F. Jensen, A. V. Lavrinenko, *Opt. Mater. Express* **2017**, 7, 1606.
- [32] Y. J. Choi, S. C. Gong, D. C. Johnson, S. Gollledge, G. Y. Yeom, H. H. Park, *Appl. Surf. Sci.* **2013**, 269, 92.
- [33] K. Liu, H. Fan, P. Ren, C. Yang, *J. Alloys Compd.* **2011**, 509, 1901.
- [34] H. A. Kramers, *Atti Cong. Intern. Fisica* **1927**, 2, 545.
- [35] R. D. L. Kronig, *JOSA* **1926**, 12, 547.
- [36] P. Drude, *Ann. Phys.* **1900**, 308, 369.
- [37] S. A. Gregory, Y. Wang, C. H. D. Groot, O. L. Muskens, *ACS Photonics* **2015**, 2, 606.
- [38] L. Y. M. Tobing, L. Tjahjana, D. H. Zhang, Q. Zhang, Q. Xiong, *Adv. Opt. Mater.* **2014**, 2, 280.
- [39] L. Y. M. Tobing, Y. Luo, K. S. Low, D. Zhang, D. H. Zhang, *Adv. Opt. Mater.* **2016**, 4, 1047.
- [40] B. Lahiri, S. G. McMeekin, A. Z. Khokhar, M. Richard, N. P. Johnson, *Opt. Express* **2010**, 18, 3210.
- [41] K. Kishor, M. N. Baitha, R. K. Sinha, B. Lahiri, *JOSA B* **2014**, 31, 1410.
- [42] A. Shabani, M. R. Roknabadi, M. Behdani, M. K. Nezhad, *Plasmonics* **2018**, 13, 1569.
- [43] L. Min, L. Huang, *Opt. Express* **2015**, 23, 19022.
- [44] T. Koschny, M. Kafesaki, E. N. Economou, C. M. Soukoulis, *Phys. Rev. Lett.* **2004**, 93, 107402.
- [45] L. Y. M. Tobing, L. Tjahjana, D. H. Zhang, Q. Zhang, Q. Xiong, *Sci. Rep.* **2013**, 3, 2437.
- [46] C. C. Chen, C. T. Hsiao, S. Sun, K. Y. Yang, P. C. Wu, W. T. Chen, Y. H. Tang, Y. F. Chau, E. Plum, G. Y. Guo, N. I. Zheludev, *Opt. Express* **2012**, 20, 9415.
- [47] J. Kim, G. V. Naik, A. V. Gavrilenko, K. Dondapati, V. I. Gavrilenko, S. M. Prokes, O. J. Glembocki, V. M. Shalaeve, A. Boltasseva, *Phys. Rev. X* **2013**, 3, 041037.
- [48] M. A. Bodea, G. Sbarcea, G. V. Naik, A. Boltasseva, T. A. Klar, J. D. Pedarnig, *Appl. Phys. A* **2013**, 110, 929.
- [49] H. Kim, M. Osofsky, S. M. Prokes, O. J. Glembocki, A. Piqué, *Appl. Phys. Lett.* **2013**, 102, 171103.
- [50] C. Stelling, C. R. Singh, M. Karg, T. A. König, M. Thelakkat, M. Retsch, *Sci. Rep.* **2017**, 7, 1.